Ultrabright Multiplexed Energy-Time-Entangled Photon Generation from Lithium Niobate on Insulator Chip

Guang-Tai Xue[1,§] Yun-Fei Niu,[1,§] Xiaoyue Liu,[2,§] Jia-Chen Duan,[1,§] Wenjun Chen,[2] Ying Pan,[2]
Kunpeng Jia,[1] Xiaohan Wang,[1] Hua-Ying Liu,[1] Yong Zhang,[1] Ping Xu,[3,1] Gang Zhao,[1]
Xinlun Cai,[2] Yan-Xiao Gong,[1,*] Xiaopeng Hu,[1,†] Zhenda Xie,[1,‡] and Shining Zhu[1]

[1]*National Laboratory of Solid State Microstructures, School of Physics, School of Electronic Science and Engineering, College of Engineering and Applied Sciences, and Collaborative Innovation Center of Advanced Microstructures, Nanjing University, Nanjing 210093, China*

[2]*State Key Laboratory of Optoelectronic Materials and Technologies and School of Physics and Engineering, Sun Yat-sen University, Guangzhou 510275, China*

[3]*Institute for Quantum Information and State Key Laboratory of High Performance Computing, College of Computing, National University of Defense Technology, Changsha 410073, China*

A high-flux entangled-photon source is a key resource for quantum optical study and application. Here, it is realized in a lithium niobate on isolator (LNOI) chip, with 2.79×10^{11} Hz/mW photon-pair rate and 1.53×10^9 Hz/(nm mW) spectral brightness. These data are boosted by over 2 orders of magnitude compared with existing technologies. A 160-nm-broad bandwidth is engineered for eight-channel multiplexed energy-time entanglement. Harnessed by high-extinction-frequency correlation and Franson interferences up to 99.17% visibility, such energy-time-entanglement multiplexing further enhances the high-flux data rate and warrants broad application in quantum-information processing on a chip.

I. INTRODUCTION

The lithium niobate (LiNbO$_3$, LN) crystal is known for its superior optical performance [1], such as low optical transmission losses and large electro-optical and second-order nonlinear coefficients. Therefore, it is used for the fabrication of top-notch optical devices for both classical and quantum-information applications. Recent progress in thin-film LN-on-insulator (LNOI) [2] technology enables a revolutionary footprint reduction of LN devices by over 3 orders of magnitude, and thus, makes a magnificent step forward towards efficient on-chip photonic integration. Various high-performance on-chip optical devices have been developed based on such LNOI chips, including low-loss waveguides [3–5], high-quality-factor microring resonators [3,5,6], and high-speed electro-optic modulators [7,8], for applications in second-harmonic generation [9–11], optical-frequency comb generation [12,13], and supercontinuum generation [14,15].

Actually, conventional waveguide devices on bulk-crystal LN wafers, with much weaker mode confinement compared with LNOI devices, already show high efficiencies and performances in the form of integrated quantum optical circuits [2,16]. Quantum states can be generated with unparalleled brightness by spontaneous parametric down conversion (SPDC), and further tailored and modulated by domain engineering [17–19] and electro-optic modulation [20–22]. Recently, important progress has been reported, which is that electro-optic modulators have been realized with over 100-GHz [7,8] bandwidth on the LNOI chip. It is not only a breakthrough in classical optical communication, but also offers the ultimate single-photon switching power that can be matched with on-chip photon flux in the order of about 100 GHz. From the nonlinear optical point of view, it is natural to expect, with emerging LNOI technologies, to push the photon-state generation and processing efficiency to that level, fulfilling the requirements of next-generation quantum optical integration. A high-brightness entangled-photon source is one of these key requirements, because it is basis for high-data-rate qubit generation, communication, and processing.

Here, we demonstrate multiplexed energy-time-entangled photon generation from a domain-engineered LNOI chip, with an ultrahigh photon-pair generation rate of 2.79×10^{11} Hz/mW that is compatible with current LNOI electro-optic modulators. Small group-velocity dispersion (GVD) is engineered in the type-zero quasi-phase-matching (QPM) [23] SPDC process in a

─────────
*gongyanxiao@nju.edu.cn
†xphu@nju.edu.cn
‡xiezhenda@nju.edu.cn
§These authors contributed equally to this work.

broad bandwidth of 160 nm, enabling eight-channel wavelength multiplexing. Franson interference is performed at each wavelength channel with visibilities of over 97%; the maximum visibility exceeds 99.17%. Our result shows the high-data-rate photon source on the LNOI chip, with both high photon flux and multiplexed energy-time entanglement, and the basis for large-scale high-density quantum-information encoding, which is key to increasing the efficiency for quantum cryptography [24,25] and frequency coding [26–30], to fulfill the need of large-scale quantum communication, quantum-information processing, and quantum simulation.

II. DESIGN AND FABRICATION OF THE DOMAIN-ENGINEERED LNOI CHIP

Photon bandwidth is the key resource for wavelength multiplexing. Here, for the type-zero QPM SPDC source in our design, a large bandwidth can be achieved by a combination of dispersion and domain engineering, enabling QPM around the zero GVD point [31,32] (see the Appendix for details). The boundary conditions of the electromagnetic field determine its effective wave vector and corresponding dispersion as well as the GVD [33,34]. For the waveguide, its boundary conditions are mainly
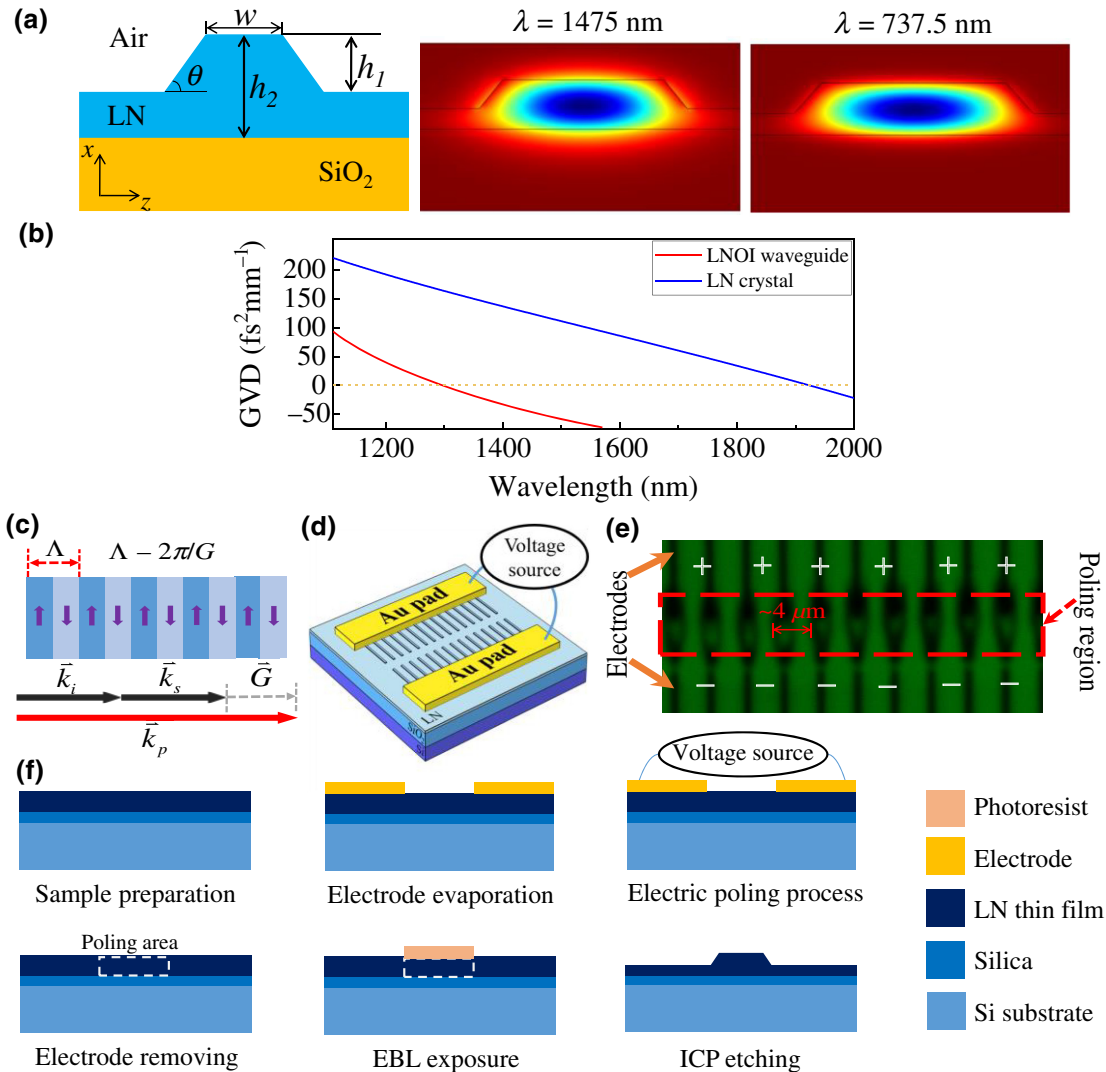

FIG. 1. Schematic of chip design and fabrication. (a) Cross section of waveguide and mode field simulation, with parameters $w = 1.4\ \mu$m, $h_1 = 350$ nm, $h_2 = 600$ nm, and $\theta = 60°$. (b) Simulation of GVD for LNOI waveguide (red line) and bulk lithium niobate crystal (blue line). (c) Quasi-phase-matching geometry, with p, s, and i denoting pump, signal, and idler fields, respectively. (d) Electrode structure and electrical field poling process. High-voltage pulses are applied along z axis of X-cut LNOI wafer. (e) Confocal laser scanning microscopy picture of domain structure. Black areas are domain walls and electrodes in poling region and outside. (f) Schematic of chip-fabrication process.

determined by the structure and size. In contrast to conventional LN waveguides, the LNOI waveguides can have high refractive-index contrast and submicron structures. The schematic of the LNOI waveguide cross section and simulation of the mode profiles are given in Fig. 1(a). By utilizing the software of COMSOL, we numerically simulate the GVD of light transmitting in the waveguide in the wavelength range from 1110 to 1570 nm. The simulated GVD for this structure is plotted in Fig. 1(b) (red). We can see that the GVD is very close to zero in the wavelength range from 1200 to 1570 nm, which is far from the zero GVD point around 1.92 μm in the bulk LN crystal, as shown in Fig. 1(b) (blue). At the working wavelength of our source, namely, 1475 nm, the GVD is about -60 fs^2/mm.

As shown in Fig. 1(c), the poling structure is designed for a degenerate type-zero SPDC process from the 737.5-nm pump to 1475-nm biphotons with a poling period of 4 μm. The fabrication process of the domain-engineered LNOI chip is illustrated in Fig. 1(f). We start from the commercial ion-sliced X-cut LNOI wafer (NANOLN) with a 600-nm lithium niobate film on 2-μm silica with 0.50-mm silicon substrate. First, the Nichrome comb electrodes and the contact Au pads shown in Fig. 1(d) are fabricated by electron-beam lithography (EBL), electron-beam evaporation, and a lift-off process. Then we use the electrical field poling technique [35] to fabricate the domain structures. Several high-voltage pulses are applied to perform a periodic domain-inversion process. A confocal microscope is used to monitor the poling quality of the LNOI chip. From the image shown in Fig. 1(e), a duty cycle of about 50% is achieved, showing high-quality fabrication. Next, the electrode is removed, and a second EBL process is performed to define the photoresist for the waveguide pattern. Finally, the waveguide structure is fabricated over the periodically poled LNOI (PPLNOI) by an inductively coupled plasma etching process, which is used to etch away the 350-nm-thick lithium niobate film. The chip length is about 8 mm, and the poling region length is 6 mm. The waveguide width is linearly tapered from 1.4 to 4.5 μm at the output port and leads to a waveguide-to-fiber-coupling efficiency of about 25% at 1550 nm.

III. SOURCE CHARACTERIZATION

We first test the PPLNOI waveguide by second-harmonic generation (SHG) to find the optimal QPM wavelengths. A tunable cw laser (Santec TSL-550) is used as the fundamental light with the power set to 0.7 mW. By tuning its wavelength, a maximum SHG light power of 4 μW is obtained after two short-pass filters (Thorlabs FESH0950), and the corresponding fundamental light wavelength is 1471.52 nm. The normalized SHG conversion efficiency is calculated to be 2270%/(W cm^2).

Based on the SHG test, we set the pump wavelength to 735.76 nm for a reverse process in SPDC to a wavelength degeneracy of around 1471.52 nm. The experimental setup of the energy-time-entangled photon-pair source is shown in Fig. 2(a), and the 735.76 nm pump light is from a tunable cw Ti:sapphire laser (M2 Sols). The PPLNOI chip is located on a temperature-controlled mount to keep the QPM temperature at 23.0 °C. We use free-space coupling for both the input and output sides of the PPLNOI chip. For the output side, the entangled photons are coupled into a single-mode fiber after passing through a long-pass filter (Thorlabs FELH0950). We build a high-performance wavelength-division multiplexing (WDM) filtering system to multiplex the energy-time entanglement, with the schematic shown in Fig. 2(b). The SPDC light is directed through a single-mode fiber to collimator A for free-space output. A set of half-wave plate (HWP) and quarter-wave plate (QWP) is used to optimize polarization for high diffraction efficiency on subsequent reflective diffraction grating $G1$. The diffracted SPDC light is then directed through a focusing lens in a $2f$ imaging setup, so that different frequency components are spatially chirped in the focal plane. A D-shaped mirror is used to reflect back the low-frequency components, and they are separated from the high-frequency components at the frequency degeneracy in the SPDC spectrum. The high-frequency components are collimated by the second lens for single-mode fiber coupling to collimator B, via a tunable reflective mirror, M, placed with a separation of f to the lens. The low-frequency components are directed back with a small angle to the input direction in the beam height, and further diffracted by a second diffraction grating, $G2$, for single-mode fiber coupling to collimator C. With angular dispersions, both collimators B and C receive 0.8-nm narrowband wavelength bins of the SPDC, and such wavelength multiplexing can be continuously turned by changing the angles of M and $G2$, respectively. This WDM filtering system covers a broad spectral range from 1350 to 1600 nm. A 3-dB insertion loss is measured for each output, with a high extinction ratio exceeding 60 dB. Utilizing this tunable WDM filtering system, we are able to pick entangled photons in any wavelength-bin pairs for measurement.

We use a coincidence measurement setup for the correlation measurements, as shown in Fig. 2(c). The single-mode-fiber coupled photon pairs are directed to and detected by a pair of SNSPDs. A fiber polarization controller is used to optimize polarization for the highest detection efficiency of the SNSPDs. The overall efficiency of the SNSPDs is around 70%, including fiber coupling, with dark counts of 3500 Hz. Coincidence measurements are performed by using the TCSPC module (Picoquant PicoHarp 300).

We first measure the SPDC generation rate by directly connecting fiber port O in Fig. 2(a) to fiber ports D_1 and
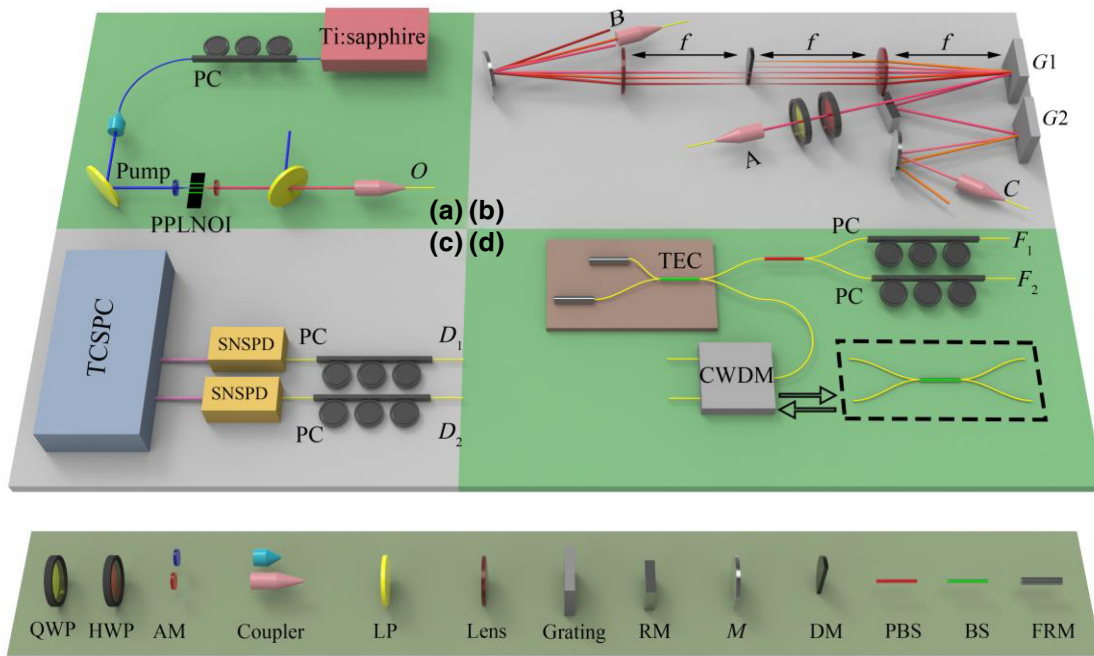
FIG. 2. Schematic of experimental setup, including following four parts: (a) energy-time-entangled photon-pair source based on PPLNOI chip, (b) tunable-wavelength division multiplexing filtering system, (c) coincidence count system, and (d) Franson interferometer to test energy-time entanglement. AM, aspheric lens; LP, long-pass filter; M, mirror; RM, rectangular mirror; DM, D-shaped mirror; PBS, polarizing beam splitter; BS, 50:50 fiber beam splitter; FRM, Faraday rotator mirror; PC, polarization controller; TEC, thermoelectric cooler; CWDM, commercial coarse-wavelength-division multiplexer; SNSPD, superconducting-nanowire single-photon detector; TCSPC, time-correlated single-photon counting. Letters O, A, B, C, D_1, D_2, F_1, and F_2 represent input or output ports of the four parts, which are separated and can be connected in different ways, as needed.

D_2 of the coincidence counting system through a 50:50 fiber beam splitter. When the pump power coupled into the waveguide is 27.8 nW, a coincidence counting rate of $R_{cc} = 4792$ Hz is measured, with an accidental coincidence counting rate of $R_{ac} = 8$ Hz. The ratio of coincidence to accidental coincidence is as high as 599. The single-photon rates at the two detectors are $R_1 = 126$ kHz and $R_2 = 295$ kHz, respectively, with a negligible dark count level of 3500 Hz. Thus, the on-chip photon-pair generation rate, $N = 2.79 \times 10^{11}$ Hz/mW, can be calculated from $N = R_1 R_2 / (R_{cc} - R_{ac})$. The heralding efficiency is calculated to be 3.8%, which is consistent with the coupling efficiency including all losses [36]. The heralding efficiency of our source is relatively low because of the low waveguide-to-fiber coupling efficiency and the transmission loss of about 10 dB in the fiber connection from the source to detectors.

To measure the spectrum brightness of the source, we connect port O in Fig. 2(a) to port A of the WDM filter in Fig. 2(b) and perform the measurement around frequency degeneracy. When the pump power coupled into the waveguide is 21.4 μW, the coincidence, accidental coincidence, and single counts are measured to be 1317 Hz, 12 Hz, 159 kHz, and 215 kHz, respectively, within the 0.8-nm bandwidth of the WDM filter. A spectrum brightness

of 1.53×10^9 Hz/(nm mW) can be calculated, which is 1–2 orders of magnitude higher than the best result of the other photon-pair sources (after normalization of the poling length) [20,37–41]. The above results fully reveal the advantage of the PPLNOI-based SPDC source with tight mode confinement. Actually, the waveguide cross-section area is 2 orders of magnitude smaller than that of the conventional lithium niobate waveguide, which is inversely proportional to the source efficiency (see the Appendix for details).

The SPDC spectrum is measured by heralded single-photon counting, where port O is connected to a 50:50 fiber coupler, with one output used for the heralding signal and the other passing the WDM filter for measurement of the spectrum. The D-shaped mirror is removed in this case, so that we can access the whole spectrum at port B. With a sweeping step of 10 nm and eliminating the effect of the variation of the coupling efficiency at different wavelengths, the SPDC spectrum shows a full width at half maximum of about 160 nm in Fig. 3(a), and the curve is fitted well with a sinc-chirped square function in agreement with our simulation (as shown in the Appendix).

With the D-shaped mirror inserted, we further measure the frequency correlation by coincidence counting for each combination of frequency-channel pairs for the signal and
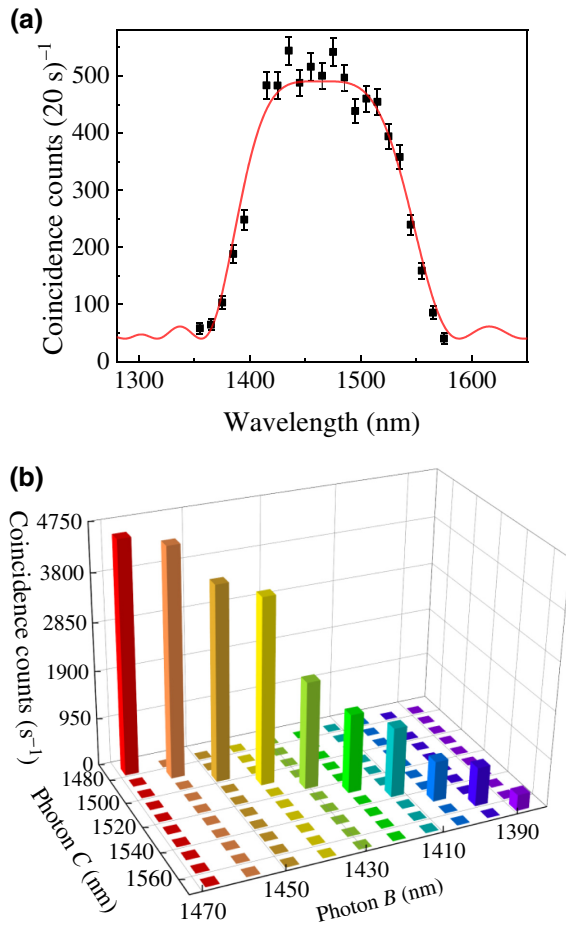
(a)

(b)

FIG. 3. Spectrum characterization of source. (a) SPDC spectrum. Black points represent coincidence counts as a function of filtering wavelength of one photon, with the other photon unfiltered. Error bars represent square roots of counts. Red solid curve is fitted with a sinc-chirped square function. (b) Frequency-correlation measurement. Coincidence counts are recorded against wavelengths of photons from couplers B and C in steps of 10 nm.

idler, and compare the coincidence rates for the correlated-frequency-channel pairs to that for the noncorrelated-frequency-channel pairs. A two-dimensional sweep is performed with the WDM filter at steps of 10 nm for ports B and C, respectively. The coincidence counting rate is plotted as a function of WDM filter wavelengths of ports B and C in Fig. 3(b). High-quality frequency anticorrelation is obtained and, explicitly, the coincidence rates are over 32 dB lower for the adjacent noncorrelated-frequency-channel pairs and 40 dB lower for nonadjacent channels.

IV. MEASUREMENT OF MULTIPLEXED ENERGY-TIME ENTANGLEMENT VIA FRANSON INTERFERENCE

The broad bandwidth and high-quality frequency correlation of the source enable the generation of

wavelength-multiplexed energy-time-entangled photon pairs, which can be harnessed using Franson interference [42] over each wavelength channel. We use only one unbalanced Michelson interferometer for the Franson measurements, where the multiplexed photon pairs are input from ports B and C of the WDM filter in Fig. 2(b) into ports F_1 and F_2 in Fig. 2(d) through fibers, respectively. Then, they are polarization controlled to be in orthogonal polarizations for the input of the Michelson interferometer, so that their relative phase difference can be easily stabilized. This Michelson interferometer is all-fiber based and is formed by a 50:50 fiber coupler, with a pair of fiber Faraday mirrors used to compensate for any unwanted polarization changes in the fiber for both long and short arms. The time imbalance of the two arms, $\Delta T = 1.5$ ns, satisfies $T_{c1} \ll \Delta T \ll T_{c2}$, where T_{c1} is the single-photon coherence time determined by the filtering bandwidth of 0.8 nm, and T_{c2} is the coherence time of the pump laser. The interferometer is placed in a temperature-controlled box with a temperature-control accuracy of 0.1 °C; and such accuracy is sufficient to change the relative phase delay, ϕ, between the two polarizations, which is distinguished by the stress-induced birefringence. Finally, the interferometer output is split and linked to ports D_1 and D_2 via a CWDM (with transition edge at 1471 nm) or a 50:50 fiber coupler for frequency-nondegenerate or degenerate photon pairs, respectively. The coincidence window, Δt, is set to 256 ps, which is smaller than the time imbalance ΔT, and hence, coincidence events for both photons taking the long arm (L-L) and short arm (S-S) can be distinguished from those for one photon in the long arm and the other in the short (L-S) arm. Due to the energy-time entanglement, the events of L-L and S-S are indistinguishable, leading to an interference effect, namely, Franson interference. Since the two photons pass the same interferometer, their path-length difference automatically falls within the single-photon coherence length for maximum Franson interference visibility. The coincidence counting rate follows a $(1 + \cos\phi)$ variation [42], with ϕ depending on the phase difference of the L-L and S-S terms controlled by the interferometer box temperature.

The Franson interference is measured for each pair of the eight wavelength channels, as marked by α_j and β_j ($j = 1, 2, \ldots, 8$), with results shown in Figs. 4(b)–4(i), respectively. All curves are fitted well using sinusoidal functions, with the corresponding visibilities listed on top, which all exceed 97%. The interference visibilities are directly calculated from raw experimental data, and the visibility error bars are calculated from the counting-rate fluctuations at the maxima and minima of the fringes, following a Poisson distribution. Although we pick only eight WDM channels for energy-time-entanglement measurements, the energy-time entanglement can actually be multiplexed in a much denser spacing, and, with the 0.8-nm WDM capability, over 100 channel pairs can
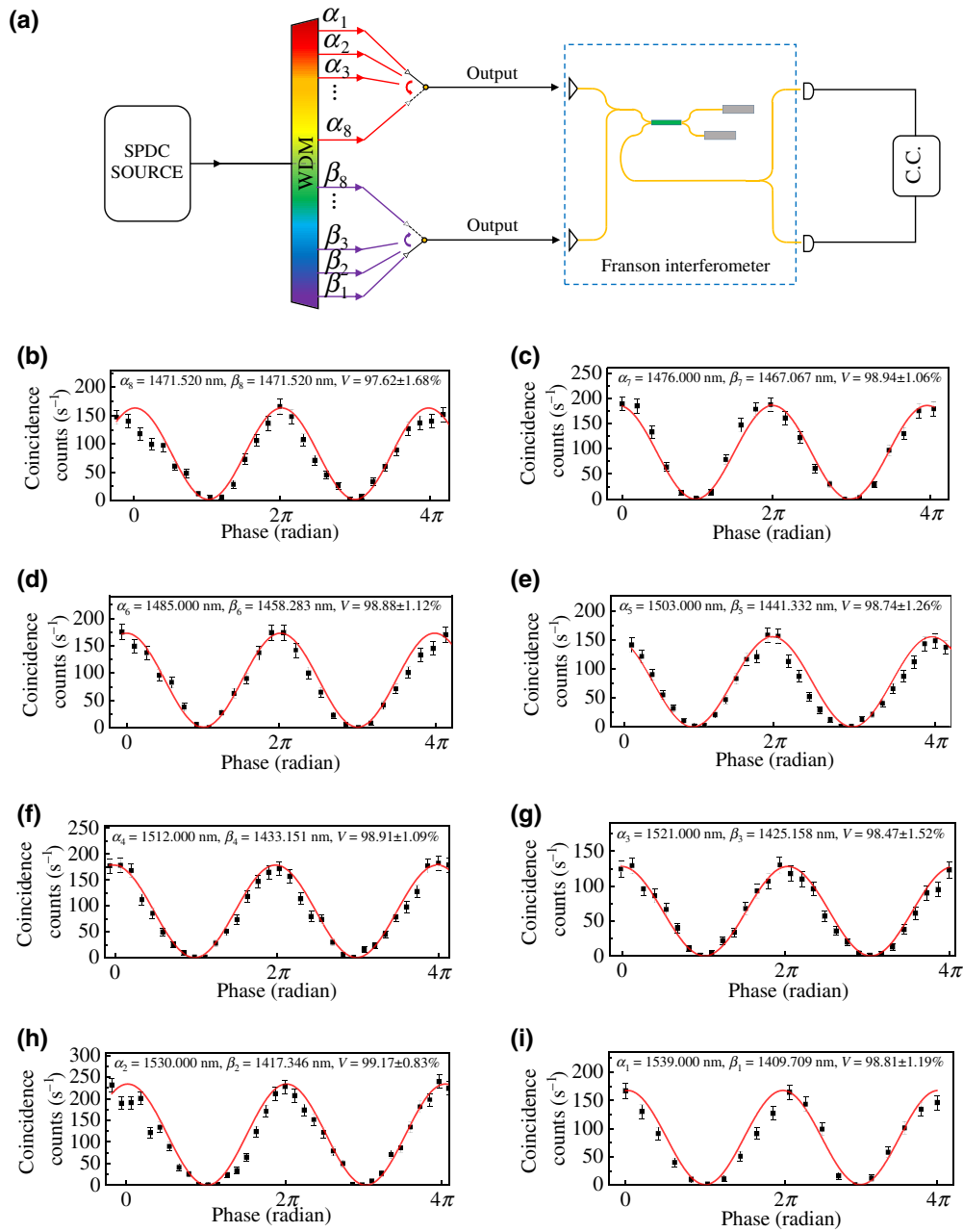
FIG. 4.   Multiplexed energy-time-entanglement characterization. (a) Illustration of multiplexed energy-time-entanglement genera-tion from our source. Franson interferences are measured for each wavelength bin after the WDM filter, with coincidence counting (C. C.) measurement. (b)–(i) Experimental results of coincidence counts for entangled photons in eight pairs of wavelength channels, α_j, β_j ($j = 1, 2, \ldots, 8$), as a function of the phase difference of both photons taking the long arm and both taking the short arm, with error bars denoting square root of counts. All curves are fitted with sine-cosine functions, with corresponding visibilities listed on top, where errors are estimated assuming Poisson fluctuation in counts.

be sliced within the 160-nm SPDC bandwidth. Together with frequency-correlation measurements, these results are sufficient to demonstrate the capability of the LNOI-based photon source for high-flux wavelength-multiplexed energy-time-entanglement generation with high fidelity, in the view of the quantum magic bullet [43].

V. DISCUSSION AND CONCLUSION

In summary, we demonstrate the multiplexed energy-time-entanglement generation in a domain-engineered LNOI chip. An ultrahigh generation rate of up to 2.79×10^{11} Hz/mW is measured. Such a high photon rate matches the potential photon-switching capability in the

order of 100 GHz, which is also possible on the same LNOI chip, for source-integrated quantum-information processing. Eight-channel wavelength multiplexing is achieved with a spectral brightness of about 10^9 Hz/(nm mW), and a high-quality frequency correlation, which has a high rejection ratio of over 32 dB for the noncorrelated-frequency-channel pairs. Franson interference is observed for all wavelength channels, and the interference visibilities are all measured to be over 97%, showing high-quality energy-time entanglement. Here, we focus on the entangled-photon-source performance from the LNOI chip and use off-chip elements for state processing and measurements. However, all devices are ready for on-chip processing, including on-chip WDMs and Franson interferometers. Hence, our approach is more than a stand-alone entangled photon source, but a breakthrough towards full-function integration of a quantum optical circuit. With the small footprints of all devices, including a high-performance photon source, a high integration density can be expected with superior photon flux, and thus, data rate in the LNOI, for the next generation of quantum-information processing chips, including quantum communication, computation, and simulation applications.

Note added.—Recently, we became aware of a related publication, see Ref. [44].

APPENDIX: CALCULATION OF THE SPECTRUM AND GENERATION RATE OF THE SOURCE

We consider a cw pump laser traveling along the waveguide with a length of L in the x direction. Since the waveguide is fabricated to be single mode for the signal and idler fields, and the pump (p) coupling is also optimized to excite the fundamental mode in the waveguide, the interaction Hamiltonian for the type-zero QPM SPDC can be treated in a single mode and written as [45]

$$H_I(t) = \varepsilon_0 \int_L dx \chi^{(2)}(x)\hat{E}_p^{(+)}(x,t)\hat{E}_s^{(-)}(x,t)\hat{E}_i^{(-)}(x,t) + \text{H.c.},$$
(A1)

where H.c. denotes the Hermitian conjugate part. The negative parts of the signal (s) and idler (i) field operators are given by

$$\hat{E}_j^{(-)}(x,t) = \int d\omega_j E_j^* e^{-i(k_j x - \omega_j t)}\hat{a}_j^\dagger(\omega_j), \quad j = s,i, \quad \text{(A2)}$$

where $E_j = i\sqrt{\hbar\omega_j/[4\pi\varepsilon_0 cn(\omega_j)]}$. The positive part of the pump (p) field operator is written as the classical field amplitude:

$$E_p^{(+)}(x,t) = E_p e^{i(k_p x - \omega_p t)}.$$
(A3)

Due to periodic poling, the second-order nonlinear susceptibility can be written in the following Fourier series:

$$\chi^{(2)}(x) = d\sum_m f_m e^{-iG_m x},$$
(A4)

where $d = d_{33}$ is the effective nonlinear coefficient; $G_m = 2m\pi/\Lambda$ is the mth-order reciprocal, with Λ denoting the poling period; and the corresponding Fourier coefficient is written as $f_m = 2/(m\pi)$ for a duty cycle of 0.5. Here, we use the first-order reciprocal, and thus, we keep only the term of $m = 1$ and can write the QPM condition as

$$\Delta k = k_p - k_s - k_i - \frac{2\pi}{\Lambda} = 0.$$
(A5)

With analogous calculations made in Refs. [36,45], we can write the frequency-degenerate SPDC state up to the first-order perturbation term as

$$|\Psi\rangle = |\text{vac}\rangle + A\int d\nu h(L\Delta k)\hat{a}_s^\dagger(\omega_{s0}+\nu)\hat{a}_i^\dagger(\omega_{i0}-\nu)|\text{vac}\rangle,$$
(A6)

where we define a frequency detuning, ν, from the central frequency, and here we consider the frequency-degenerate case, namely, $\omega_{s0} = \omega_{i0} = \omega_p/2$, with ω_p denoting the pump frequency. The joint spectrum amplitude, $h(L\Delta k)$, is determined by the phase-matching function, which is written as

$$h(L\Delta k) = \exp\left(-i\frac{L\Delta k}{2}\right)\text{sinc}\left(\frac{L\Delta k}{2}\right).$$
(A7)

The coefficient A absorbs all constants and slowly varying functions of frequency, as given by [36]

$$A = i\frac{1}{3}\sqrt{\frac{2}{\pi^3}}\frac{n_{g0}d_{33}LE_p\omega_p}{cn_0^2},$$
(A8)

where n_{g0} and n_0 represent the group refractive index and the refractive index of light at frequency $\omega_p/2$, respectively.

To further investigate the source spectrum, we expand the signal and idler wave vectors around the central frequencies up to the second order in the detuning v, respectively,

$$
\begin{aligned}
k_s(\omega_s &= \omega_p/2 + v) \\
&= \frac{n(\omega_p/2 + v)}{c} \approx \frac{n_0\omega_p}{2c} + \frac{1}{u_0}v + \frac{g_0}{2}v^2, \quad \text{(A9)}
\end{aligned}
$$

$$
\begin{aligned}
k_i(\omega_i &= \omega_p/2 - v) \\
&= \frac{n(\omega_p/2 - v)}{c} \approx \frac{n_0\omega_p}{2c} - \frac{1}{u_0}v + \frac{g_0}{2}v^2, \quad \text{(A10)}
\end{aligned}
$$

where u_0 and g_0 are the group velocity and group velocity dispersion of light at frequency $\omega_p/2$, which are expressed as

$$
u_0 = \frac{d\omega}{dk}\bigg|_{\omega=\omega_p/2}, \quad \text{(A11)}
$$

$$
g_0 = \frac{d^2k}{d\omega^2} = \frac{d}{dk}\left(\frac{1}{u}\right)\bigg|_{\omega=\omega_p/2}. \quad \text{(A12)}
$$

Since the QPM condition given by Eq. (A5) is satisfied for signal and idler photons at $\omega_p/2$, we can obtain

$$
\Delta k = k_p - k_s - k_i - \frac{2\pi}{\Lambda} \approx -g_0v^2. \quad \text{(A13)}
$$

Hence, the spectrum amplitude given by Eq. (A7) can be estimated up to the second order in v as

$$
h(L\Delta k) = \exp\left(-i\frac{Lg_0}{2}v^2\right)\text{sinc}\left(\frac{Lg_0}{2}v^2\right). \quad \text{(A14)}
$$

With one photon triggered without spectrum analysis, the spectrum amplitude of the other photon can be obtained as

$$
P(v) = |h(L\Delta k)|^2 = \text{sinc}^2\left(\frac{Lg_0}{2}v^2\right), \quad \text{(A15)}
$$

and alternatively, as a function of wavelength it is written as

$$
P(\lambda) = \text{sinc}^2\left[2\pi^2c^2Lg_0\left(\frac{1}{\lambda} - \frac{1}{2\lambda_p}\right)^2\right], \quad \text{(A16)}
$$

which is proportional to the coincidence count for the spectrum measurement shown in Fig. 3(a). By utilizing the numerical simulation made in Fig. 1(d), and $\lambda_p = 735.76$ nm, $L = 6$ mm, and $g_0 = -60$ fs^2/mm, we plot the spectrum amplitude against wavelength in Fig. 5, from which we can calculate the FWHM to be about 200 nm, which is larger than the experimental result of 160 nm due to deviation from the theoretical design.
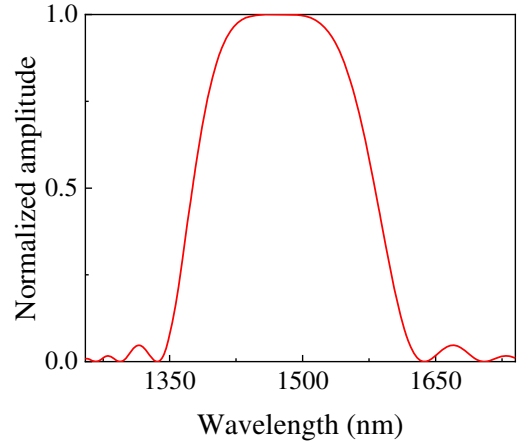

FIG. 5. Simulation of source spectrum based on theoretical design.

The photon-pair generation rate (PGR) can be obtained by calculating the trace of the two-photon term of the state given by Eq. (A6) as

$$
R = |A|^2 \int dv|h(L\Delta k)|^2. \quad \text{(A17)}
$$

Substituting Eqs. (A8), (A14), and $|E_p|^2 = 2P/(\varepsilon_0 n_p cS)$, we obtain

$$
R = \frac{64Pd_{33}^2 n_{g0}^2}{27\pi\varepsilon_0 cS\lambda_p^2 n_0^4 n_p}\sqrt{\frac{2\pi L^3}{|g_0|}}, \quad \text{(A18)}
$$

where S is the effective cross-section area of the pump [36], and here it is the cross-section area of the LNOI waveguide. We can see that the generation rate is inversely proportional to the area. Since the area of the LNOI waveguide is 1–2 orders of magnitude smaller than that of the conventional lithium niobate waveguide, the generation rate can be also increased 1–2 orders of magnitude. With $\lambda_p = 735.76$ nm, $P = 1$ mW, $S = 1.26$ μm^2, $L = 6$ mm, $d_{33} = 33$ pm/V, $g_0 = -60$ fs^2/mm, $n_{g0} = 2.28$, $n_0 = 1.95$, and $n_p = 2.18$, we obtain the PGR as $R = 3.56 \times 10^{11}$ Hz/mW.

Due to fabrication errors, including the LNOI itself, the structures of our experimental samples deviate from the theoretical design, resulting in a larger $|g|$; therefore, the experimentally measured PGR is lower than that obtained in the theoretical calculation. We replace $|g_0|$ with about 95 fs^2/mm (as deduced from the experimentally measured SPDC spectrum) and obtain the PGR as $R = 2.83 \times 10^{11}$ Hz/mW, which is very close to the value directly measured experimentally.

[1] R. S. Weis and T. K. Gaylord, Lithium niobate: Summary of physical properties and crystal structure, Appl. Phys. A **37**, 191 (1985).

[2] A. Boes, B. Corcoran, L. Chang, J. Bowers, and A. Mitchell, Status and potential of lithium niobate on insulator (LNOI) for photonic integrated circuits, Laser Photonics Rev. **12**, 1700256 (2018).

[3] R. Wu, M. Wang, J. Xu, J. Qi, W. Chu, Z. Fang, J. Zhang, J. Zhou, L. Qiao, Z. Chai, *et al.*, Long low-loss-litium niobate on insulator waveguides with sub-nanometer surface roughness, Nanomaterials **8**, 910 (2018).

[4] I. Krasnokutska, J. J. Tambasco, X. Li, and A. Peruzzo, Ultra-low loss photonic circuits in lithium niobate on insulator, Opt. Express **26**, 897 (2018).

[5] M. Zhang, C. Wang, R. Cheng, A. Shams-Ansari, and M. Lončar, Monolithic ultra-high-Q lithium niobate microring resonator, Optica **4**, 1536 (2017).

[6] J. Lin, Y. Xu, Z. Fang, M. Wang, J. Song, N. Wang, L. Qiao, W. Fang, and Y. Cheng, Fabrication of high-Q lithium niobate microresonators using femtosecond laser micromachining, Sci. Rep. **5**, 8072 (2015).

[7] C. Wang, M. Zhang, X. Chen, M. Bertrand, A. Shams-Ansari, S. Chandrasekhar, P. Winzer, and M. Lončar, Integrated lithium niobate electro-optic modulators operating at CMOS-compatible voltages, Nature **562**, 101 (2018).

[8] M. He, M. Xu, Y. Ren, J. Jian, Z. Ruan, Y. Xu, S. Gao, S. Sun, X. Wen, L. Zhou, *et al.*, High-performance hybrid silicon and lithium niobate Mach–Zehnder modulators for 100 gbit s^{-1} and beyond, Nat. Photonics **13**, 359 (2019).

[9] R. Luo, Y. He, H. Liang, M. Li, and Q. Lin, Highly tunable efficient second-harmonic generation in alithium niobate nanophotonic waveguide, Optica **5**, 1006 (2018).

[10] C. Wang, C. Langrock, A. Marandi, M. Jankowski, M. Zhang, B. Desiatov, M. M. Fejer, and M. Lončar, Ultrahigh-efficiency wavelength conversion in nanophotonic periodically poled lithium niobate waveguides, Optica **5**, 1438 (2018).

[11] J. Lin, N. Yao, Z. Hao, J. Zhang, W. Mao, M. Wang, W. Chu, R. Wu, Z. Fang, L. Qiao, *et al.*, Broadband Quasi-Phase-Matched Harmonic Generation in an On-Chip Monocrystalline Lithium Niobate Microdisk Resonator, Phys. Rev. Lett. **122**, 173903 (2019).

[12] M. Zhang, B. Buscaino, C. Wang, A. Shams-Ansari, C. Reimer, R. Zhu, J. Kahn, and M. Lončar, Broadband electro-optic frequency comb generation in a lithium niobate microresonator, Nature **568**, 373 (2019).

[13] C. Wang, M. Zhang, R. Zhu, H. Hu, and M. Lončar, Monolithic lithium niobate photonic circuits for Kerr frequency comb generation and modulation, Nat. Commun. **10**, 978 (2019).

[14] J. Lu, J. B. Surya, X. Liu, Y. Xu, and H. X. Tang, Octave-spanning supercontinuum generation in nanoscale lithium niobate waveguides, Opt. Lett. **44**, 1492 (2019).

[15] M. Yu, B. Desiatov, Y. Okawachi, A. L. Gaeta, and M. Lončar, Coherent two-octave-spanning supercontinuum generation in lithium-niobate waveguides, Opt. Lett. **44**, 1222 (2019).

[16] J. Wang, F. Sciarrino, A. Laing, and M. G. Thompson, Integrated photonic quantum technologies, Nat. Photonics **14**, 273 (2020).

[17] S. Tanzilli, H. De Riedmatten, H. Tittel, H. Zbinden, P. Baldi, M. De Micheli, D. B. Ostrowsky, and N. Gisin, Highly efficient photon-pair source using periodically poled lithium niobate waveguide, Electron. Lett. **37**, 26 (2001).

[18] P. Xu and S. N. Zhu, Review Article: Quasi-phase-matching engineering of entangled photons, AIP Adv. **2**, 041401 (2012).

[19] H. Jin, P. Xu, X. W. Luo, H. Y. Leng, Y. X. Gong, W. J. Yu, M. L. Zhong, G. Zhao, and S. N. Zhu, Compact Engineering of Path-Entangled Sources From a Monolithic Quadratic Nonlinear Photonic Crystal, Phys. Rev. Lett. **111**, 023603 (2013).

[20] H. Jin, F. M. Liu, P. Xu, J. L. Xia, M. L. Zhong, Y. Yuan, J. W. Zhou, Y. X. Gong, W. Wang, and S. N. Zhu, On-Chip Generation and Manipulation of Entangled Photons Based on Reconfigurable Lithium-Niobate Waveguide Circuits, Phys. Rev. Lett. **113**, 103601 (2014).

[21] F. Lenzini, J. Janousek, O. Thearle, M. Villa, B. Haylock, S. Kasture, L. Cui, H.-P. Phan, D. V. Dao, H. Yonezawa, *et al.*, Integrated photonic platform for quantum information with continuous variables, Sci. Adv. **4**, eaat9331 (2018).

[22] K.-H. Luo, S. Brauner, C. Eigner, P. R. Sharapova, R. Ricken, T. Meier, H. Herrmann, and C. Silberhorn, Nonlinear integrated quantum electro-optic circuits, Sci. Adv. **5**, eaat1451 (2019).

[23] J. A. Armstrong, N. Bloembergen, J. Ducuing, and P. S. Pershan, Interactions between light waves in a nonlinear dielectric, Phys. Rev. **127**, 1918 (1962).

[24] D. Aktas, B. Fedrici, F. Kaiser, T. Lunghi, L. Labonte, and S. Tanzilli, Entanglement distribution over 150 km in wavelength division multiplexed channels for quantum cryptography, Laser Photonics Rev. **10**, 451 (2016).

[25] S. Wengerowsky, S. Koduru Joshi, F. Steinlechner, H. Hübel, and R. Ursin, An entanglement-based wavelength-multiplexed quantum communication network, Nature **564**, 225 (2018).

[26] Z. Xie, T. Zhong, S. Shrestha, X. Xu, J. Liang, Y.-X. Gong, J. C. Bienfang, A. Restelli, J. H. Shapiro, F. N. C. Wong, and C. W. Wong, Harnessing high-dimensional hyperentanglement through a biphoton frequency comb, Nat. Photonics **9**, 536 (2015).

[27] J. M. Lukens and P. Lougovski, Frequency-encoded photonic qubits for scalable quantum information processing, Optica **4**, 8 (2017).

[28] W.-T. Fang, Y.-H. Li, Z.-Y. Zhou, L.-X. Xu, G.-C. Guo, and B.-S. Shi, On-chip generation of time-and wavelength-division multiplexed multiple time-bin entanglement, Opt. Express **26**, 12912 (2018).

[29] P. Imany, J. A. Jaramillo-Villegas, M. S. Alshaykh, J. M. Lukens, O. D. Odele, A. J. Moore, D. E. Leaird, M. Qi, and A. M. Weiner, High-dimensional optical quantum logic in large operational spaces, npj Quantum Inf. **5**, 59 (2019).

[30] C. Reimer, S. Sciara, P. Roztocki, M. Islam, L. R. Cortés, Y. Zhang, B. Fischer, S. Loranger, R. Kashyap, A. Cino, *et al.*, High-dimensional one-way quantum processing implemented on d-level cluster states, Nat. Phys. **15**, 148 (2019).

[31] O. Prakash, H. H. Lim, B. J. Kim, K. Pandiyan, M. Cha, and B. Rhee, Collinear broadband optical parametric generation in periodically poled lithium niobate crystals by group velocity matching, Appl. Phys. B **92**, 535 (2008).

[32] M. Levenius, V. Pasiskevicius, F. Laurell, and K. Gallo, Ultra-broadband optical parametric generation in periodically poled stoichiometric LiTaO$_3$, Opt. Express **19**, 4121 (2011).

[33] B. E. A. Saleh and M. C. Teich, *Fundamentals of Photonics*, 3rd ed. (John Wiley & Sons, Hoboken, Wiley, 2019).

[34] R. Boyd, *Nonlinear Optics*, 3rd ed. (Elsevier, Singapore, 2009).

[35] S. N. Zhu, Y. Y. Zhu, Z. Y. Zhang, H. Shu, H. F. Wang, J. F. Hong, C. Z. Ge, and N. B. Ming, LiTaO$_3$ crystal periodically poled by applying an external pulsed field, J. Appl. Phys. **77**, 5481 (1995).

[36] J. Schneeloch, S. H. Knarr, D. F. Bogorin, M. L. Levangie, C. C. Tison, R. Frank, G. A. Howland, M. L. Fanto, and P. M. Alsing, Introduction to the absolute brightness and number statistics in spontaneous parametric down-conversion, J. Opt. **21**, 043501 (2019).

[37] N. Montaut, L. Sansoni, E. Meyer-Scott, R. Ricken, V. Quiring, H. Herrmann, and C. Silberhorn, High-Efficiency Plug-and-Play Source of Heralded Single Photons, Phys. Rev. Appl. **8**, 024021 (2017).

[38] C.-W. Sun, S.-H. Wu, J.-C. Duan, J.-W. Zhou, J.-L. Xia, P. Xu, Z. Xie, Y.-X. Gong, and S.-N. Zhu, Compact polarization-entangled photon-pair source based on a dual-periodically-poled Ti : LiNbO$_3$ waveguide, Opt. Lett. **44**, 5598 (2019).

[39] X. Guo, C. L. Zou, C. Schuck, H. Jung, R. Cheng, and H. X. Tang, Parametric down-conversion photon-pair source on a nanophotonic chip, Light Sci. Appl. **6**, e16249 (2017).

[40] C. Ma, X. Wang, V. Anant, A. D. Beyer, M. D. Shaw, and S. Mookherjea, Silicon photonic entangled photon-pair and heralded single photon generation with CAR > 12,000 and $g^{(2)}(0) < 0.006$ Opt. Express **25**, 32995 (2017).

[41] C. Clausen, F. Bussières, A. Tiranov, H. Herrmann, C. Silberhorn, W. Sohler, M. Afzelius, and N. Gisin, A source of polarization-entangled photon pairs interfacing quantum memories with telecom photons, New J. Phys. **16**, 093058 (2014).

[42] J. D. Franson, Bell Inequality for Position and Time, Phys. Rev. Lett. **62**, 2205 (1989).

[43] S. Lloyd, J. H. Shapiro, and F. N. C. Wong, Quantum magic bullets by means of entanglement, J. Opt. Soc. Am. B **19**, 312 (2002).

[44] J. Zhao, C. Ma, M. Rüsing, and S. Mookherjea, High Quality Entangled Photon Pair Generation in Periodically Poled Thin-Film Lithium Niobate Waveguides, Phys. Rev. Lett. **124**, 163603 (2020).

[45] Y.-X. Gong, Z.-D. Xie, P. Xu, X.-Q. Yu, P. Xue, and S.-N. Zhu, Compact source of narrow-band counterpropagating polarization-entangled photon pairs using a single dual-periodically-poled crystal, Phys. Rev. A **84**, 053825 (2011).